



## NRC Publications Archive Archives des publications du CNRC

### **Diffuse interface tracking of immiscible fluids : improving phase continuity through free energy density selection**

Donaldson, A. A.; Kirpalani, D. M.; Macchi, A.

This publication could be one of several versions: author's original, accepted manuscript or the publisher's version. / La version de cette publication peut être l'une des suivantes : la version prépublication de l'auteur, la version acceptée du manuscrit ou la version de l'éditeur.

For the publisher's version, please access the DOI link below. / Pour consulter la version de l'éditeur, utilisez le lien DOI ci-dessous.

#### **Publisher's version / Version de l'éditeur:**

<https://doi.org/10.1016/j.ijmultiphaseflow.2011.02.002>

*International Journal of Multiphase Flow*, 37, pp. 777-787, 2011-04-01

#### **NRC Publications Record / Notice d'Archives des publications de CNRC:**

<https://nrc-publications.canada.ca/eng/view/object/?id=43fdc6f4-70c8-42df-9f15-caf46c4e6c1a>

<https://publications-cnrc.canada.ca/fra/voir/objet/?id=43fdc6f4-70c8-42df-9f15-caf46c4e6c1a>

Access and use of this website and the material on it are subject to the Terms and Conditions set forth at

<https://nrc-publications.canada.ca/eng/copyright>

READ THESE TERMS AND CONDITIONS CAREFULLY BEFORE USING THIS WEBSITE.

L'accès à ce site Web et l'utilisation de son contenu sont assujettis aux conditions présentées dans le site

<https://publications-cnrc.canada.ca/fra/droits>

LISEZ CES CONDITIONS ATTENTIVEMENT AVANT D'UTILISER CE SITE WEB.

**Questions?** Contact the NRC Publications Archive team at

PublicationsArchive-ArchivesPublications@nrc-cnrc.gc.ca. If you wish to email the authors directly, please see the first page of the publication for their contact information.

**Vous avez des questions?** Nous pouvons vous aider. Pour communiquer directement avec un auteur, consultez la première page de la revue dans laquelle son article a été publié afin de trouver ses coordonnées. Si vous n'arrivez pas à les repérer, communiquez avec nous à PublicationsArchive-ArchivesPublications@nrc-cnrc.gc.ca.





## Diffuse interface tracking of immiscible fluids: Improving phase continuity through free energy density selection

A.A. Donaldson<sup>a,b</sup>, D.M. Kirpalani<sup>a,\*</sup>, A. Macchi<sup>b</sup>

<sup>a</sup> Institute for Chemical Process and Environmental Technology, National Research Council Canada, <sup>1</sup> M-12, 1200 Montreal Road, Ottawa, Ontario, Canada K1A 0R6

<sup>b</sup> Dept. of Chemical and Biological Engineering, University of Ottawa, 161 Louis Pasteur Street, Ottawa, Ontario, Canada K1N 6N5

### ARTICLE INFO

#### Article history:

Received 31 May 2010

Received in revised form 23 December 2010

Accepted 2 February 2011

Available online 1 April 2011

#### Keywords:

Diffuse-interface method

Phase-field

Interface tracking

Cahn–Hilliard free energy theory

Continuity

Spontaneous drop shrinkage

Critical drop radius

### ABSTRACT

Diffuse interface (DI) tracking methods frequently adopt the double-well energy density function to describe the free energy variation across an interface, leading to phase interpenetration and spontaneous drop shrinkage when applied to immiscible two-phase systems. While the observed continuity losses can be limited by constraints placed on the interfacial width and mobility parameter, the associated increase in computational cost and mesh requirements has limited DI methods to 2D planar and axi-symmetric flow.

Using the proposed temperature-variant simplified energy density function (TVSED), the effect of the metastable thermodynamic region on phase continuity is examined using a reduced temperature parameter,  $T_R$ . The solutions obtained by the proposed DI implementation and a volume-of-fluid (VOF) based solver are discussed for two common benchmark simulations (collapse of a column of water, and droplet deformation/relaxation in simple shear). While comparable solutions are obtained from the  $T_R = 0$  and VOF simulations; the large metastable region of the more commonly used double-well function ( $T_R = 1$ ) promoted inter-mixing in the bulk phases, diluting the inertia transferred between impacting fluids and under-predicting deformation in shear. The fundamental mechanisms responsible for spontaneous drop shrinkage are eliminated at  $T_R = 0$ , allowing for constraints on the interfacial width and mobility to be relaxed. The comparable performance of  $T_R = 0$  and VOF simulations is a promising indication of the potential for application to complex 3D flows at reduced mesh resolution relative to existing DI methods.

Crown Copyright © 2011 Published by Elsevier Ltd. All rights reserved.

### 1. Introduction

Over the last decade, the diffuse interface (DI) method for multi-phase computational fluid dynamics (CFD) has been applied successfully to a variety of physical systems involving extensive topological changes and length scales commensurate with the thickness of the interface. Following the early stages of development (refer to the review by Anderson et al. (1998)), applications of the DI method have generally followed the works of Jacqmin (1999) and Badalassi et al. (2003), with modifications made to incorporate high density ratio fluids (Inamuro et al., 2004; Yuan and Schaefer, 2006; Takada and Tomiyama, 2006; Ding et al., 2007) and multi-component systems (Kim, 2007). Extensions of the DI method to incompressible two-phase flow have provided insight into a variety of flow phenomena, including the impact (Khatavkar et al., 2007) and spreading (Ding et al., 2007) of droplets on treated surfaces, and droplet breakup in micro-fluidic geometries (De Menech, 2006). Despite the continued evolution of the DI

method, a number of inherent limitations exist due to the nature of the Cahn–Hilliard dynamics governing interfacial transport: spontaneous drop shrinkage and a perceived loss of continuity (Yue et al., 2007), increased grid resolution requirements relative to sharp-interface tracking methods, and limited applicability to complex geometries and unstructured meshes due to spatial discretization requirements.

The interface between fluids in the DI method is described as a finite region across which physical and thermodynamic properties are resolved. Transport of this region is governed by the convective Cahn–Hilliard equation (Cahn and Hilliard, 1958, 1959), where the equilibrium profile of the order parameter used to delineate between phases is maintained through the minimization of free energy. Restorative diffusive fluxes are driven by gradients in the chemical potential, which are governed by the function selected to describe the bulk free energy density (Jacqmin, 1999). The double-well function is commonly used for its numerical simplicity, approximating the van der Waals Equation of State for highly-miscible mixtures near the critical point. When the location of an interface is visualized by a contour of the volume fraction ( $\phi = 0.5$ ), a gradual loss of continuity is observed. This perceived continuity loss is caused by a combination of three mechanisms:

\* Corresponding author. Tel.: +1 613 991 6958; fax: +1 613 991 2384.

E-mail address: [Deepak.kirpalani@nrc-cnrc.gc.ca](mailto:Deepak.kirpalani@nrc-cnrc.gc.ca) (D.M. Kirpalani).

<sup>1</sup> NRCC No: 52855.

energy exchange between the interface and bulk that results in spontaneous drop shrinkage (Yue et al., 2007); initial conditioning and curvature induced losses due to discrepancies between the one-dimensional and actual equilibrium profile; and interfacial smearing during advection (Jacqmin, 1999; Yue et al., 2004; Feng et al., 2005). While global continuity of  $\phi$  is maintained, the loss of continuity of the volume bounded by the  $\phi = 0.5$  contour can lead to the incorrect interpretation of results, poor resolution of surface forces across an interface, variations in the physical properties of the bulk fluids as the phases interpenetrate, and the disappearance of small droplets.

With a few exceptions discussed by Zhou et al. (2010), the mesh resolution necessary to mitigate the aforementioned limitations has led to the use of 2D planar or axisymmetric geometries in the majority of reported literature. Nonetheless, many engineering problems involve complex 3D geometries and multi-phase flow where 2D and 3D dynamics differ significantly (viscous encapsulation, spray formation, multi-phase micro-fluidic contactors). The inherent ability of the DI method to regularize singular events such as breakup, coalescence and moving contact lines has led to several attempts at 3D implementation within a framework that is practical both in complexity and computational cost (Badalassi et al., 2003; Jacqmin, 2004; Zhou et al., 2010). Each of these implementations has attempted to either minimize the number of cells across the interface using high-order and spectral discretization, or minimize the total mesh size through adaptive mesh refinement in the vicinity of the interface. The first approach has limited application in complex geometries, where the order of the spatial discretization techniques used is limited on unstructured meshes. The second approach requires additional cells across the interface to accurately resolve free energy variations and surface force contributions given the reduced order of the spatial discretization schemes available on unstructured meshes common to adaptive mesh refinement algorithms. Additional strategies have been suggested to minimize the perceived continuity loss, including guidelines for selecting the mobility parameter governing the magnitude of diffusive fluxes (Yue et al., 2007), and limiting the width of the interfacial region (Jacqmin, 1999). While each of the reported approaches improved control over the extent of continuity loss within a quiescent system, such approaches may require significant mesh refinement. Additionally, such methods do not consider the mechanisms responsible for continuity loss in convective flow.

Alternative energy functions for partially miscible or immiscible fluids are available in previous literature, such as the double-obstacle function (Langer et al., 1975; Oono and Puri, 1988) or equations of state (Yuan and Schaefer, 2006; Takada and Tomiyama, 2006). These functions typically have a larger spinodal thermodynamic region and smaller metastable region, limiting the extent of phase inter-mixing and improving the rate at which the equilibrium profile of the order parameter is restored when deformed. Aside from the limitations in applying an energy function for highly miscible fluids to describe the interaction of two immiscible fluids, the increased numerical complexity associated with the implementation of alternative energy functions has resulted in the continued use of the double-well function in most recent applications (Anderson et al., 1998; Jacqmin, 1999; Badalassi et al., 2003; De Menech, 2006; Ding et al., 2007; Kim, 2007; Zhou et al., 2010). In order to apply the DI approach to 3D simulations of fluid flow through complex geometries, the mechanisms responsible for continuity loss must be addressed without incurring excessive computational cost through mesh refinement.

In this work, a temperature-variant simplified energy density function (TVSED) is proposed for describing a range of simplified energy density expressions transitioning from the double-well to the double-obstacle function. Through the variation of a parameter akin to the reduced temperature, the effects of the metastable

thermodynamic region and inter-phase miscibility on spontaneous drop shrinkage and loss of continuity are explored. In order to maintain a numerical complexity comparable to that of approaches using the double-well function, a modified form of the Cahn–Hilliard equation is proposed in conjunction with a diffusive flux limiting methodology, minimizing variations of the order parameter that are beyond the bulk-phase values. The proposed method is then applied to two-phase benchmark cases to compare the relative performance of the double-well function and an energy function with no metastable region.

## 2. Free energy theory for interface tracking

In the DI method, the equilibrium state of a binary mixture is governed by the minimization of the Helmholtz free-energy,  $H[\phi]$ , defined using the Ginzburg–Landau functional as:

$$H[\phi] = \int_V \frac{\lambda}{\varepsilon^2} \left\{ f(\phi) + \frac{\varepsilon^2}{2} |\nabla \phi|^2 \right\} dV \quad (2.1)$$

where  $\lambda$  is the mixing energy density,  $\varepsilon$  is the capillary width of the interface,  $f(\phi)$  is the bulk free energy density, and  $0.5\varepsilon^2|\nabla\phi|^2$  is the excess free energy due to the presence of an interface.

The thermodynamic properties of the bulk free energy has a significant effect on the computational behavior of the interface: controlling phase miscibility, separation dynamics and the extent of inter-mixing between phases. Equations of state (EOS)-based functions were originally used for their clear thermodynamic basis and the ability to vary inter-phase miscibility through a temperature parameter (Yuan and Schaefer, 2006). However, they are avoided in Eulerian interface tracking studies due to the added complexity of implementation resulting from variable minimum energy states and stability constraints on  $\phi$  (Takada and Tomiyama, 2006). Instead, simplified expressions are generally used to approximate the free energy variation at specific thermodynamic conditions.

The double-well function, shown in Eq. (2.2), is the simplest of the non-singular expressions for  $f(\phi)$ .

$$f(\phi) = 0.25\phi^2(1 - \phi)^2 \quad (2.2)$$

Originally developed as an approximation of the van der Waals equation at near-critical conditions, it was adopted by a number of interface tracking algorithms due to its numerical simplicity (Anderson et al., 1998; Jacqmin, 1999; Badalassi et al., 2003; De Menech, 2006; Ding et al., 2007; Kim, 2007). For the simple case of a planar interface separating two phases, the one-dimensional equilibrium profile can be derived from energy-minimization considerations, and expressed as:

$$\phi = 0.5 + 0.5 \tanh \left( \frac{x}{\sqrt{2}\varepsilon} \right) \quad (2.3)$$

where the capillary width and mixing energy density are defined as:

$$\varepsilon = \frac{\psi}{2\sqrt{2}} \arctan h(1 - 2\varphi) \quad (2.4)$$

$$\lambda = \frac{3}{2\sqrt{2}} \varepsilon \sigma \quad (2.5)$$

In the above expressions,  $\psi$  is the thickness of the interface on the computational domain,  $\sigma$  is the surface tension, and  $\varphi$  is the filtering parameter governing the extent of the interfacial region ( $\varphi \leq 1 - \varphi$ ), commonly set at  $\varphi = 0.05$  for the double-well function.

Alternative energy density expressions for immiscible fluid systems have been proposed in the past, such as the double-obstacle function for immiscible fluids (Langer et al., 1975; Oono and Puri, 1988).

$$f(\phi) = \begin{cases} 0.5\phi(1-\phi) & 0 < \phi < 1 \\ \infty & \phi \geq 1, \phi \leq 0 \end{cases} \quad (2.6)$$

Or the following function having square-root behavior in the bulk phases:

$$f(\phi) = |\phi|^{3/2} |1-\phi|^{3/2} \quad (2.7)$$

These expressions are typically avoided due to the additional numerical complexity arising in the treatment of the bulk phases (Jacqmin, 1999).

The double-well and double-obstacle functions represent two extremes of thermodynamic behavior and phase miscibility. In an effort to compare these functions on a common numerical framework, a temperature-variant simplified energy density (TVSED) function is proposed with thermodynamic properties comparable to the van der Waals EOS.

$$f(\phi) = |\phi(1-\phi)|^{1+T_R} \quad (2.8)$$

As the reduced temperature parameter,  $T_R$ , varies from  $T_R = 1$  at the critical point to  $T_R = 0$  for immiscible fluids,  $f(\phi)$  transitions from the double-well to the double-obstacle function within the  $0 < \phi < 1$  region. From free energy considerations, the one-dimensional equilibrium profile, capillary width and mixing energy density can be derived and expressed as:

$$x = \varepsilon 2^{T_R-0.5} (1-2\phi) {}_2F_1 \left[ \frac{1}{2}, \frac{1+T_R}{2}; \frac{3}{2}; (1-2\phi)^2 \right] \quad (2.9)$$

$$\varepsilon = \frac{\psi}{2^{T_R+0.5} (1-2\phi) {}_2F_1 \left[ \frac{1}{2}, \frac{1+T_R}{2}; \frac{3}{2}; (1-2\phi)^2 \right]} \quad (2.10)$$

$$\lambda = \sigma \varepsilon 2^{T_R+0.5} \left[ {}_2F_1 \left[ \frac{1}{2}, -\frac{(1+T_R)}{2}; \frac{3}{2}; 1 \right] \right]^{-1} \quad (2.11)$$

where  ${}_2F_1[a_1, a_2; b_1; z]$  is the hypergeometric function:

$${}_2F_1[a_1, a_2; b_1; z] = 1 + \sum_{k=0}^{\infty} c_k \frac{c_k}{c_{k-1}} = \frac{(k+a_1)(k+a_2)}{(k+b_1)(k+1)} z, \quad c_{-1} = 1 \quad (2.12)$$

A graphical comparison of the thermodynamic behavior of the van der Waals, double-well, double-obstacle and TVSED functions can be found in the accompanying electronic annex.

### 3. Equations of motion

#### 3.1. Convective Cahn–Hilliard equation

The transport and reconstruction of the diffuse interface between two fluids, denoted A and B, is governed by the convective Cahn–Hilliard equation (Cahn and Hilliard, 1958, 1959):

$$\frac{\partial \phi}{\partial t} + \nabla \cdot (u\phi) + \nabla \cdot (I\mathbf{J}) = 0 \quad (3.1)$$

Similar to sharp interface methods, the volume fraction of phase A is frequently applied as the order parameter delineating between phases,  $\phi$ . The temporal evolution of  $\phi$  is dependent on convective transport due to the divergence-free volume-averaged velocity,  $\mathbf{u}$ , and diffusive transport due to gradients in the chemical potential,  $\mu = -\delta H[\phi]/\delta \phi$ . The magnitude of the diffusive term is controlled by the mobility parameter,  $\Gamma$ , and the diffusive volumetric flux,  $\mathbf{J}$ , which is a function of the gradient of the chemical potential. The non-dimensional form of Eq. (3.1) incorporates the mobility parameter into a Péclet number, necessitating the selection of a characteristic velocity. In this work, an alternative approach is proposed for the TVSED to address the numerical instabilities that arise in the treatment of the bulk phases for  $T_R < 1$ .

When interfacial diffusion is dominant over bulk diffusion (Langer et al., 1975), the mobility is defined as a function of the order parameter,  $\Gamma = \Gamma_C |\phi(1-\phi)|$ , in which the critical mobility,  $\Gamma_C$ , governs the temporal stability of diffusive transport. Through an analogy to convective transport, a diffusive Courant number,  $C_T$ , is proposed to determine a suitable value for  $\Gamma_C$  given the characteristic grid cell length and time step,  $\Delta x$  and  $\Delta t$  respectively.

$$C_T = \Delta t \max \left\{ \frac{1}{\Delta x} \frac{I\mathbf{J}}{\phi} \right\} \quad (3.2)$$

The advantage of this approach becomes apparent for the non-dimensional form of Eq. (3.1), where the time scale of diffusive transport is no longer coupled to a characteristic velocity through the Péclet number.

To determine the magnitude of  $\Gamma_C$  and diffusive transport, the diffusive flux is calculated from the gradient of the chemical potential:

$$\mathbf{J} = -\nabla \mu = \frac{\lambda}{\varepsilon^2} (\varepsilon^2 \nabla (\nabla^2 \phi) - f''(\phi) \nabla \phi) \quad (3.3)$$

The restorative diffusivity,  $f''(\phi)$ , is determined from the second derivative of  $f(\phi)$  with respect to  $\phi$ . For the TVSED,  $f''(\phi)$  has the following form:

$$f''(\phi) = (1+T_R) \{T_R - (4T_R+2)[\phi(1-\phi)]\} |\phi(1-\phi)|^{T_R-1} \quad (3.4)$$

For values of  $T_R < 1$ ,  $f''(\phi)$  is numerically unstable in the bulk regions where  $\phi(1-\phi) = 0$ . This instability can be eliminated through a combination and rearrangement of the diffusive flux and mobility to obtain the following expression for  $I\mathbf{J}$ :

$$I\mathbf{J} = \Gamma_C \frac{\lambda}{\varepsilon^2} \text{pos}[\phi(1-\phi)] \{[\phi(1-\phi)] \varepsilon^2 \nabla (\nabla^2 \phi) - \zeta(\phi) \nabla \phi\} \quad (3.5)$$

In which  $\text{pos}[\phi(1-\phi)] = 1$  for  $\phi(1-\phi) \geq 0$  and zero for negative values, and  $\zeta(\phi)$  is defined as:

$$\zeta(\phi) = (1+T_R) (T_R - (4T_R+2)[\phi(1-\phi)]) |\phi(1-\phi)|^{T_R} \quad (3.6)$$

Incorporating Eq. (3.5) into the expression for  $C_T$  and rearranging for the critical mobility at  $\phi = 0.5$  yields:

$$\Gamma_C = \frac{C_T \varepsilon^2}{\Delta t 2\lambda} \left[ \max \left\{ \frac{1}{\Delta x} \left( \frac{\varepsilon^2}{4} \nabla (\nabla^2 \phi) + \frac{(1+T_R)}{2^{2T_R+1}} \nabla \phi \right) \right\} \right]^{-1} \quad (3.7)$$

Through the use of Eqs. (3.1), (3.5), and (3.7), the proposed TVSED function can be implemented as a diffuse interface tracking algorithm for which phase miscibility is varied to determine the effects on continuity. Note that similar to existing diffuse interface approaches, the interface is visualized by a  $\phi = 0.5$  contour.

#### 3.2. Momentum equation

The incompressible Navier–Stokes equation and continuity equation can be expressed for a two-phase mixture with variable viscosity and density as:

$$\rho \frac{\partial \mathbf{u}}{\partial t} + \rho \mathbf{u} \cdot \nabla \mathbf{u} = -\nabla p + \nabla \cdot (\eta (\nabla \mathbf{u} + \nabla \mathbf{u}^T)) + F_S + \rho \mathbf{g} \quad (3.8)$$

$$\nabla \cdot \mathbf{u} = 0 \quad (3.9)$$

where  $p$  and  $\mathbf{g}$  are the pressure and acceleration due to gravity,  $F_S$  is the surface force, and  $\rho$  and  $\eta$  are the density and viscosity, defined as a function of the order parameter and the bulk-phase values:

$$\rho(\phi) = \rho_A \phi + \rho_B (1-\phi) \quad (3.10)$$

$$\eta(\phi) = \eta_A \phi + \eta_B (1-\phi) \quad (3.11)$$

The continuous surface force formulation proposed by Kim (2005) for the DI approach was originally considered, approximating  $F_S$  as:

$$F_S = -\lambda \nabla \cdot \left( \frac{\nabla \phi}{|\nabla \phi|} \right) |\nabla \phi| \nabla \phi \quad (3.12)$$

While validated extensively for the double-well function, the use of Eq. (3.12) with the TVSED function is complicated by the increased linearity of the equilibrium profile as  $T_R \rightarrow 0$ . Consider the relative magnitudes of  $|\nabla \phi| \nabla \phi$  for an interface at  $T_R = 1$  and  $T_R = 0$ . At  $T_R = 1$ , 92% of the surface forces are concentrated within the four central cells of a 60cell interface. At  $T_R = 0$ ,  $|\nabla \phi| \nabla \phi$  is more widely distributed, and 5.2 cells are required to account for the same percentage of surface forces. The wider distribution leads to better estimates of  $|\nabla \phi| \nabla \phi$  using lower-order discretization schemes; however, the surface force contributions extend closer to the center of the radius of curvature, where the reduced tangential linearity of  $\phi$  causes an increase in error associated to the curvature approximation,  $\nabla \cdot (\nabla \phi / |\nabla \phi|)$ .

To improve the performance of Kim's formulation at  $T_R = 0$ , the interfacial profile was linearized and an arbitrary energy function applied for the calculation of  $|\nabla \phi| \nabla \phi$ . For the  $T_R = 0$  equilibrium profile of  $\phi = 0.5 + 0.5 \sin(\min(\max(\sqrt{2}x/\varepsilon, -\pi/2), \pi/2))$ , the linearized order parameter was expressed as  $\phi' = \arcsin(2\phi - 1)$ . In addition, an arbitrary energy function was applied through the following surface force formulation:

$$F_S = -\lambda' \nabla \cdot \left( \frac{\nabla \phi'}{|\nabla \phi'|} \right) |\nabla \phi'| \nabla \phi' [\phi(1 - \phi)]^{2n} \quad (3.13)$$

where  $n$  governed the distribution of the surface forces and  $\lambda'$  is a modified mixing energy:

$$\lambda' = \frac{\varepsilon \sigma}{\sqrt{2}} \left[ \int_0^1 [\phi(1 - \phi)]^{2n-0.5} d\phi \right]^{-1} \quad (3.14)$$

Values of  $n = 0.5$  and  $n = 0.75$  approximate the traditional surface force distributions at  $T_R = 0$  and  $T_R = 1$  respectively. Higher values of  $n$  centralize the surface forces, where  $n \geq 1.5$  results in greater than 99.9% of the surface forces being accounted for within the  $\phi \leq \phi \leq 1 - \phi$  region. A value of  $n = 1.75$  ( $\lambda' = 140\varepsilon\sigma/\sqrt{2}$ ) was found to yield favorable spurious current convergence rates and pressure rise error with mesh refinement during the simulation of a stagnant droplet (see accompanying [electronic annex](#) for complete details). Based on these results,  $F_S$  was approximated using Eq. (3.12) for  $T_R = 1$  and Eq. (3.13),  $n = 1.75$  for  $T_R = 0$ .

#### 4. Numerical procedure

Numerical simulations carried out using OpenFOAM<sup>®</sup>, an open-source math-based solver for computational fluid dynamics on unstructured meshes, employed a staggered grid approach with scalar variables and fluxes defined at cell centers and cell faces respectively. The time stepping procedure was based on a 4th order explicit Runge–Kutta (ERK4) multi-step approach solving Eqs. (3.1) and (3.8) consecutively with a flux-limiting correction step to prevent over/under-shoots in  $\phi$ . A detailed outline of the numerical approach can be found in the accompanying [electronic annex](#). Although the simulations in Section 5 are two-dimensional, OpenFOAM only requires modification of the mesh to extend to three-dimensions.

#### 5. Results and discussion

##### 5.1. Spontaneous shrinkage of quiescent droplets

When implemented with the double-well function, the DI method is subject to spontaneous drop shrinkage, whereby the Cahn–Hilliard dynamics reduces the total free energy in a system through an exchange between interfacial and bulk energies (Yue

et al., 2007). As a result of this exchange, the interfacial position of a droplet with initial radius,  $r_o$ , shifts to a lower radius,  $r$ , until the total free energy is minimized. Through the analysis of free energy variation with droplet radius, Yue et al. (2007) proposed an expression for a critical initial radius,  $r_c$ , for which a droplet with  $r_o < r_c$  will eventually disappear:

$$r_c \approx \left( \frac{\sqrt{6}}{8\pi} V \varepsilon \right)^{1/3} \quad (5.1)$$

Derived for the double-well function,  $r_c$  is dependent on the volume of the computational domain,  $V$ , and the capillary width,  $\varepsilon = \psi/4.164$ .

A similar analysis was completed for the TVSED function. For a given droplet radius, the total free energy can be derived through the integration of  $H[\phi]$  over the computational domain:

$$H(r, T_R) = 2\pi r \sigma + \frac{\lambda}{\varepsilon^2} \left\{ |[1 + \partial\phi](1 - [1 + \partial\phi])|^{T_R+1} \pi r^2 + |[ \partial\phi](1 - [ \partial\phi])|^{T_R+1} (V - \pi r^2) \right\} \quad (5.2)$$

In this equation,  $\partial\phi$  represents the shift in the bulk value of  $\phi$  and can be expressed as:

$$\partial\phi = \frac{\pi(r_o^2 - r^2)}{V} \quad (5.3)$$

Neglecting  $\partial\phi$  terms of order greater than two, the temperature-dependent total free energy can be simplified and approximated as:

$$H(r, T_R) \approx 2\pi r \sigma + \frac{\lambda}{\varepsilon^2} \frac{\pi^{T_R+1}}{V^{T_R}} |r_o^2 - r^2|^{T_R+1} \quad (5.4)$$

The surface tension,  $\sigma$ , is obtained from Eq. (2.11). The critical radius corresponds to the value of  $r$  for which  $\partial H(r, T_R) / \partial r = 0$  at the inflection point of  $H(r, T_R)$ , determined to be  $r_i = r_o / \sqrt{2T_R + 1}$  for a 2D droplet through the solution of  $\partial^2 H(r, T_R) / \partial r^2 = 0$ . Solving for the critical radius at  $r = r_i$ :

$$r_c = \left[ \frac{\sqrt{1+2T_R}}{\sqrt{2}(T_R+1)} \left( \frac{1+2T_R}{4T_R} \frac{V}{\pi} \right)^{T_R} \varepsilon_2 F_1 \left[ \frac{1}{2}, -\frac{(1+T_R)}{2}; \frac{3}{2}; 1 \right] \right]^{\frac{1}{2T_R+1}} \quad (5.5)$$

The critical radius of a three-dimensional droplet can also be derived, for which  $r_i = r_o(3T_R + 1)^{-1/3}$ :

$$r_c = \left[ \frac{\sqrt{2}(1+3T_R)^{1/3}}{(1+T_R)} \left( \frac{1+3T_R}{T_R} \frac{V}{8\pi} \right)^{T_R} \varepsilon_2 F_1 \left[ \frac{1}{2}, -\frac{(1+T_R)}{2}; \frac{3}{2}; 1 \right] \right]^{\frac{1}{3T_R+1}} \quad (5.6)$$

The variation of  $H(r, T_R)$  with  $T_R$  for a droplet with initial radius  $r_o = 0.1$  m,  $\psi = 0.04164$  m,  $\sigma = 0.05$  N m<sup>-1</sup> and  $V = 4$  m<sup>3</sup> is illustrated in Fig. 1. Under these conditions, the critical droplet radius at  $T_R = 1$  is  $r_c = 0.157$  m. As expected, the droplet would vanish at  $T_R = 1$  due to the absence of a minimum energy state at a radius above the inflection point in  $H(r, T_R)$ . As  $T_R$  decreases, a minimum energy state is introduced above the inflection point in Fig. 1, limiting the extent of drop shrinkage. At  $T_R = 0$ , the initial and minimum energy states converge, eliminating the mechanism responsible for the spontaneous drop shrinkage phenomenon. This result illustrates that the shrinkage phenomena greatly depends on the choice of energy function rather than being an inherent characteristic of Cahn–Hilliard dynamics.

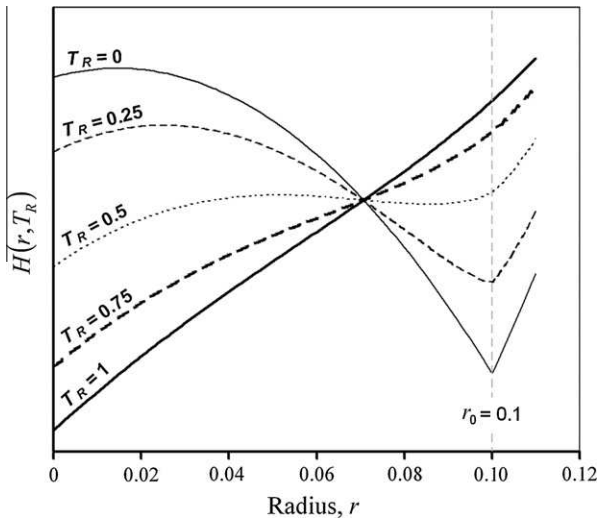


Fig. 1. Temperature dependency of the radial variation in total free energy for a 2D droplet with initial radius,  $r_0 = 0.1$  m.  $\psi = 0.04164$  m,  $\sigma = 0.05$  N m<sup>-1</sup>.

5.2. Metastable thermodynamics and phase separation

As an interface tracking technique, the phase-field approach relies on the competing mechanisms of diffusive transport to maintain the equilibrium profile for  $\phi$ . The separation dynamics governing the reconstruction of an interface are dependent on the thermodynamic regions of the energy density function. Rapid phase separation occurs within the spinodal region while gradual phase separation or mixing can occur in the metastable region.

A classic example illustrating the poor separation dynamics of the double-well function involves the absorption of a smaller droplet by a larger adjacent droplet via transfer of  $\phi$  through the metastable region. To examine this test case, two droplets with initial radii of 12 and 24 cells were placed at  $(x, y) = (64, 32)$  and  $(64, 84)$  respectively on a  $128 \times 128$  computational domain with  $\phi = 0.05$ ,  $\psi = 6$  cells,  $C_T = 0.001$ ,  $\Delta t = 0.001$  s and  $\sigma = 1$  N m<sup>-1</sup>. Fig. 2 illustrates the initial, transient and final interfacial profiles for simulations carried out at  $T_R = 0$  and  $T_R = 1$  until steady-state solutions were obtained. As shown in Fig. 2, the smaller droplet was gradually absorbed by the larger droplet at  $T_R = 1$ . During the droplet absorption, the two adjacent interfaces were connected by a mixture within the metastable thermodynamic region, having

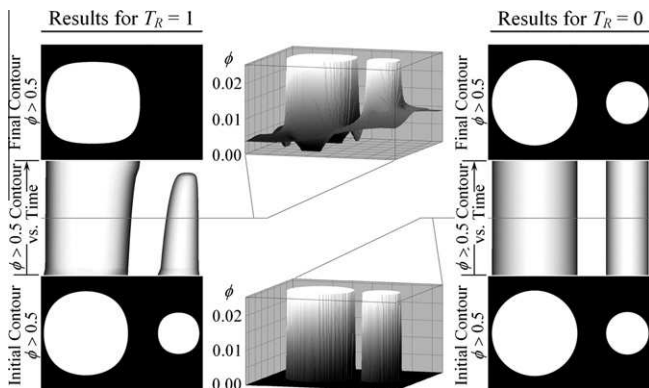


Fig. 2. Effect of  $T_R$  on the non-physical adsorption of an adjacent droplet arising from transport through the metastable region. Transient behavior and  $\phi$  profiles obtained for simulation parameters:  $\phi = 0.05$ ,  $\psi = 6$  cells,  $C_T = 0.001$ ,  $\Delta t = 0.001$  s and  $\sigma = 1$  N m<sup>-1</sup>.

typical values of  $\phi$  less than 0.01. The total free energy of the system was then minimized by a diffusive flux of  $\phi$  through this region, resulting in the gradual absorption of the smaller droplet. In the case of  $T_R = 0$ , this metastable mixture was absent, and the two drops remain in their original condition throughout the simulation.

These results illustrate the importance of the choice of energy function for interface tracking applications, in which the formation of metastable mixtures could have a significant impact on the validity of the results obtained. The remainder of this discussion focuses on comparing the solutions obtained using  $T_R = 0$  and  $T_R = 1$  for a number of cases commonly used to validate interface tracking capabilities, free surface flows and the interaction between surface forces and shear stress.

5.3. Interface tracking and phase continuity

Of the three mechanisms leading to continuity loss, previous literature has frequently considered only the initial relaxation of the 1D equilibrium profile and the spontaneous drop shrinkage phenomena (Jacqmin, 1999; Yue et al., 2004; Feng et al., 2005). Phase inter-mixing and continuity loss during convection was characterized as an extension of the dynamics governing spontaneous drop shrinkage under quiescent conditions (Yue et al., 2007). To explore the effect of the metastable region on phase inter-mixing, diagonal convection simulations were carried out using the TVSED function at  $T_R = 0$  and  $T_R = 1$ .

A circular region with a 16-cell radius was initialized at the center of a  $128 \times 128$  cyclic computational domain using Eq. (2.10) with  $\phi = 0.05$ ,  $\psi = 6$  cells,  $C_T = 0.001$ ,  $\Delta t = 7.8125 \times 10^{-6}$  s (convective flow Courant number,  $C_U = 0.001$ ), and  $\sigma = 1$  N m<sup>-1</sup>. Applying a quiescent velocity field ( $u = v = 0$  m s<sup>-1</sup>), the initial  $\phi$  profile was conditioned through the solution of Eq. (2.1) until a steady-state droplet radius was achieved. The projected area of the computational domain for which  $\phi \geq 0.5$  was measured and compared to that of the initialized case to determine the loss of continuity observed. Fig. 3 and 4 show the continuity loss during conditioning for  $T_R = 0$  and  $T_R = 1$  respectively. For both  $T_R = 0$  and  $T_R = 1$ , a rapid loss of continuity was observed during the first few time steps as the one-dimensional equilibrium profile predicted by Eq. (2.10) relaxed to account for grid-dependent discretization error. This initial conditioning resulted in 0.175% and 0.488% continuity loss for  $T_R = 0$  and  $T_R = 1$  respectively. A steady-state, relaxed solution was obtained for  $T_R = 0$  by  $t = 1$  s, with a minimal loss in continuity

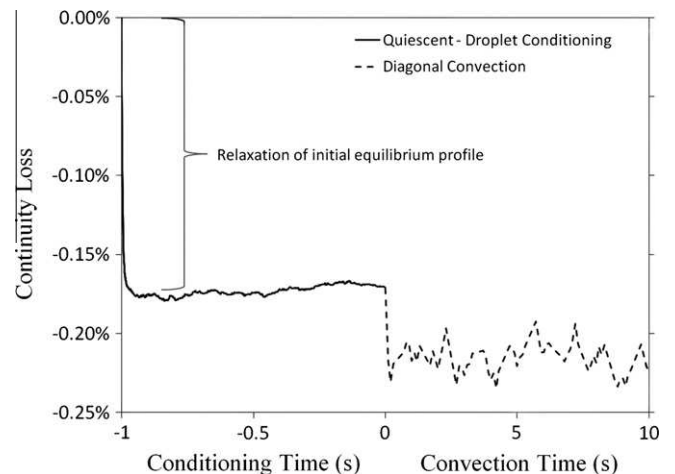
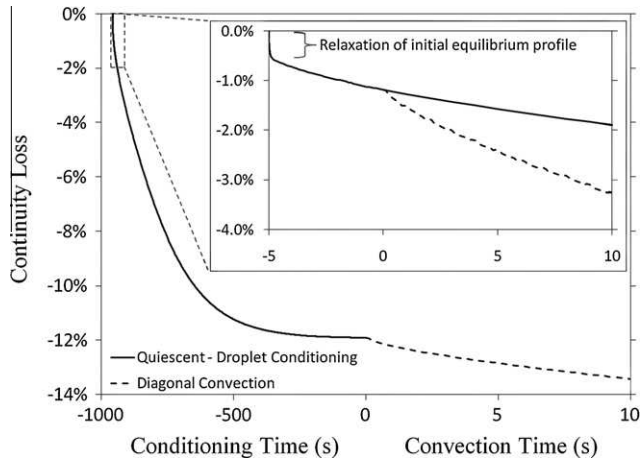
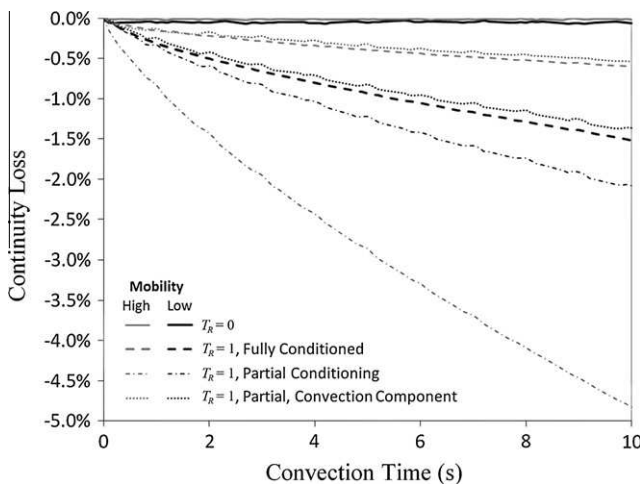


Fig. 3. Continuity loss of a circular region during relaxation and diagonal convection at  $T_R = 0$ . Other simulation parameters:  $128 \times 128$  mesh,  $r_0 = 16$  m,  $\phi = 0.05$ ,  $\psi = 6$  m,  $C_T = 0.001$ ,  $C_U = 0.001$ ,  $\sigma = 1$  N m<sup>-1</sup>.



**Fig. 4.** Continuity loss of a circular region during partial (inset) and full relaxation, and diagonal convection at  $T_R = 1$ . Other simulation parameters:  $128 \times 128$  mesh,  $r_o = 16$  m,  $\phi = 0.05$ ,  $\psi = 6$  m,  $C_I = 0.001$ ,  $C_U = 0.001$ ,  $\sigma = 1$  N m $^{-1}$ .

beyond that already observed during the first few time steps. The simulation for  $T_R = 1$  did not reach a fully conditioned solution until  $t \cong 950$  s, at which point the total continuity loss was 11.91%. The quiescent simulation results shown in Figs. 3 and 4 illustrate the elimination of the spontaneous drop shrinkage phenomena at  $T_R = 0$ , with the only observable continuity loss occurring due to the relaxation of the initial one-dimensional equilibrium profile. Applying a  $u = v = 128$  m s $^{-1}$  velocity field, continuity loss was monitored during diagonal convection of the fully conditioned  $T_R = 0$  and  $T_R = 1$  quiescent solutions. As seen in Fig. 3, minimal continuity loss was observed during convection for  $T_R = 0$ . When  $T_R = 1$  (Fig. 4), gradual loss of continuity occurred with each traversal of the computational domain, despite a steady-state solution having already been obtained under quiescent conditions. To characterize any synergistic effects between spontaneous drop shrinkage and metastable mixing, the simulation was repeated at  $T_R = 1$  for the case where the initial system was only partially conditioned ( $t_{conditioning} = 5$  s). As shown in Fig. 5, the overall continuity loss was higher for the partially conditioned solution than the fully conditioned solution. However, when the continuity loss under quiescent conditions for the same time period was accounted for, the remaining



**Fig. 5.** Effects of  $T_R$  and mobility (low,  $C_I = 0.001$ ; high,  $C_I = 0.01$ ) on continuity loss during diagonal convection of fully and partially conditioned systems. Other simulation parameters:  $128 \times 128$  mesh,  $r_o = 16$  m,  $\phi = 0.05$ ,  $\psi = 6$  m,  $C_U = 0.001$ ,  $\sigma = 1$  N m $^{-1}$ .

convective component of the partially conditioned solution’s continuity loss was almost identical to that of the fully conditioned simulation for  $T_R = 1$ . This confirms that the metastable mixing mechanism responsible for convective continuity loss is independent of the spontaneous drop shrinkage phenomenon.

The convection simulations were repeated with a mobility courant number of  $C_I = 0.01$  to characterize the effects of increasing the relative magnitude of the diffusive flux on spontaneous drop shrinkage and metastable mixing. For  $T_R = 1$ , the convective component of continuity loss improved significantly for both the partially and fully conditioned cases. However, the improvement in the partially conditioned case was offset by the acceleration of spontaneous drop shrinkage, leading to a net increase in continuity loss of 2.75% over that observed at  $C_I = 0.001$ .

Taking into account the extended length of time required for the  $T_R = 1$  simulation to reach a relaxed solution, one might argue that the continuity loss observed in a shorter simulation would be minimal. Yue et al. (2007) provided guidelines to this effect, suggesting limits on the mobility and a reduction in the Cahn number to reduce the extent of continuity loss within a given time frame. Even with these guidelines in place, continuity losses above 1% are not uncommon when reported in literature (Yue et al., 2005, 2007). The use of these guidelines is further limited by the increased grid requirements and smaller time steps needed to avoid interfacial smearing during convection when the mobility and Cahn number are reduced. The proposed TVSED function avoids this issue as  $T_R \rightarrow 0$ , with the only significant source of continuity loss arising from the initial relaxation of the one-dimensional equilibrium profile.

5.4. Free surface flow: collapse of a liquid column

Scientific literature on conventional-scale free surface flows is dominated by sharp-interface tracking techniques, where the low relative magnitude of surface forces does not justify the increased computational cost associated with a DI approach. Nonetheless, the performance of new interface tracking techniques is frequently benchmarked using free surface flow systems, such as the collapse of a liquid column under gravity (Koshizuka and Oka, 1996; Kim and Lee, 2003; Sochnikov and Efrima, 2003; Yue et al., 2003; Bonet et al., 2004; Cruchaga et al., 2007). Using the experimental data of Cruchaga et al. (2007), Koshizuka and Oka (1996) and Martin and Moyce (1952), the interface tracking capabilities of the VOF model built into OpenFOAM® and the TVSED function at  $T_R = 0$  and  $T_R = 1$  were compared for the case of a collapsing column of water with initial width,  $L = 0.114$  m, and aspect ratio,  $A_R = H/L = 2$ .

The computational domain illustrated in Fig. 6 was adapted from experiments by Cruchaga et al. (2007), in which the flow was described for both the initial collapse and subsequent settling of a column of water. Simulations were performed on a  $140 \times 210$  mesh with no-slip boundary conditions on the bottom and side

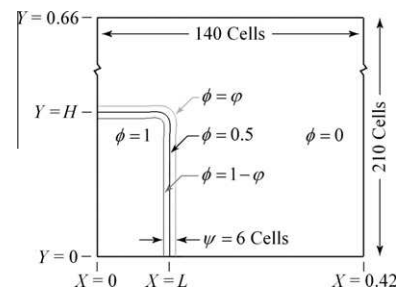


**Fig. 6.** Case description of a collapsing column of water ( $\phi = 1$ ) in air ( $\phi = 0$ ) with initial width,  $L = 0.114$  m, and aspect ratio,  $A_R = H/L = 2$ .

walls. Each case was initialized using the 1D equilibrium profile and conditioned through the solution of Eq. (3.1) for 1000 time steps with  $C_T = 0.01$ . After initial conditioning, simulations were carried out with the following fluid properties and parameters:  $C_T = 0.01$ ,  $C_U = \Delta t U / \Delta x = 0.001$ ,  $\rho_{liq} = 1000 \text{ kg m}^{-3}$ ,  $\eta_{liq} = 0.001 \text{ Pa s}$ ,  $\rho_{gas} = 1.2 \text{ kg m}^{-3}$ ,  $\psi = 0.018 \text{ m}$  and  $\sigma = 0.072 \text{ N m}^{-1}$ . Simulations were performed at a gas viscosity equal to the liquid viscosity,  $\eta_{gas} = \eta_{liq}$  (HV), as suggested by Cruchaga et al. (2007), and at the real viscosity of air,  $\eta_{gas} = 0.01\eta_{liq}$  (LV). A low value was used for the Courant number based on convective flow velocity,  $C_U$ , to minimize temporal discretization error and to maximize the relative magnitude of restorative diffusive fluxes.

Defined as the point where the  $\phi = 0.5$  contour intersects the bottom wall, the predicted leading edge position of the collapsing column was found to be similar for the VOF,  $T_R = 0$  and  $T_R = 1$  simulations (Fig. 7). The results of each model compared well with experimental data as well as alternative interface tracking techniques reported in literature for the initial collapse of a liquid column with  $A_R = 2$  (Martin and Moyce, 1952; Takada and Tomiyama, 2006; Takada et al., 2006; Cruchaga et al., 2007). However, following the initial collapse and contact of the leading edge with the wall ( $X = 0.42 \text{ m}$ ), significant differences were observed between the VOF and TVSED predictions. Using the VOF model as a benchmark, the results for  $T_R = 0$  were consistently closer than those of  $T_R = 1$ . The position of the leading edge in Fig. 7 was higher at  $T_R = 0$  due to a degree of inter-mixing at  $T_R = 1$  in the high curvature region near the top-corner of the column.

In Fig. 8, the peak heights for  $T_R = 0$  were closer to those of the VOF model near  $t = 1 \text{ s}$ , with both simulations predicting an intermediate peak just before the large peak at  $t = 2 \text{ s}$ . The VOF and  $T_R = 0$  simulations both predicted a greater dimensionless height close to  $t = 1$  in Fig. 9 due to a recession of the interface from the wall at  $X = 0.42 \text{ m}$ . Such similarities were also observed in Figs. 10 and 11, whereas the results for  $T_R = 1$  differed due to spontaneous drop shrinkage and shearing of the interface after  $t \approx 0.4 \text{ s}$ .

As shown in Fig. 11, the VOF method predicted the formation of a thin column of droplets that eventually fall and impact with the interface at the base of the wall. Similar results were obtained for  $T_R = 0$ , where the small droplets observed in the VOF simulation appeared as a partial interface along the wall since the grid resolution was insufficient to resolve each droplet. The eventual impact of the droplets caused the interface to recede away from the base of the wall, corresponding to the minima shown in Fig. 10 near  $t = 1 \text{ s}$ . Despite the formation of a partial interface along the wall, there was

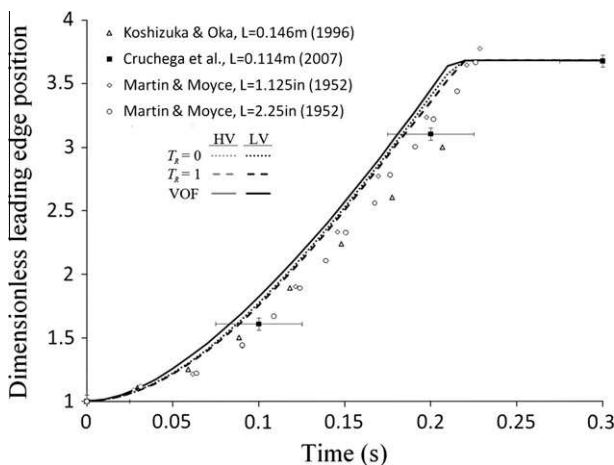


Fig. 7. Dimensionless leading edge position,  $X/L$ , of a collapsing water column with aspect ratio,  $A_R = 2$ , obtained using the TVSED function and a VOF method with a high air viscosity,  $0.001 \text{ Pa s}$  (HV), and a low air viscosity,  $0.00001 \text{ Pa s}$  (LV).

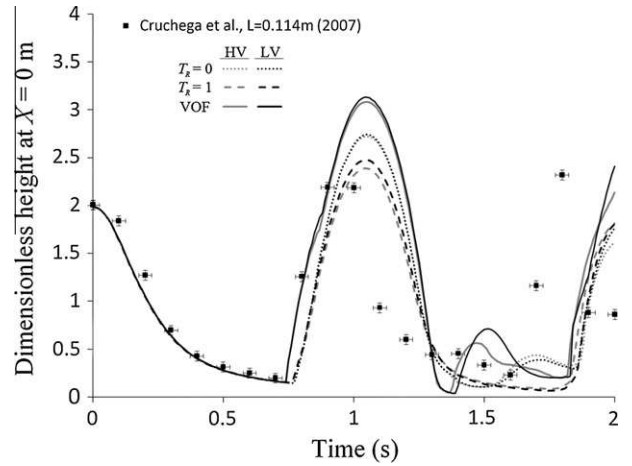


Fig. 8. Dimensionless height,  $Y/L$ , of a collapsing water column at  $X = 0 \text{ m}$ .

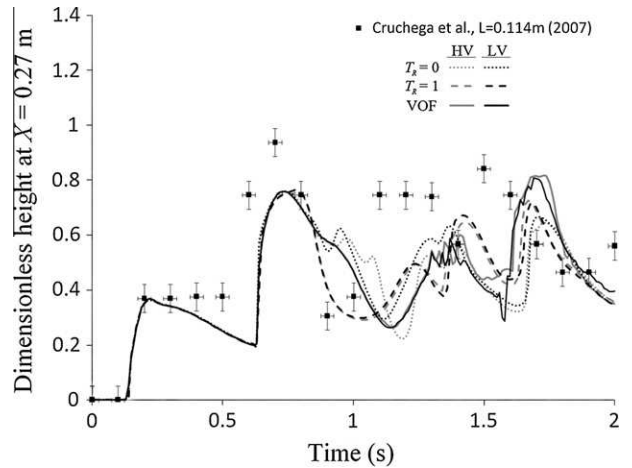


Fig. 9. Dimensionless height,  $Y/L$ , of a collapsing water column at  $X = 0.27 \text{ m}$ .

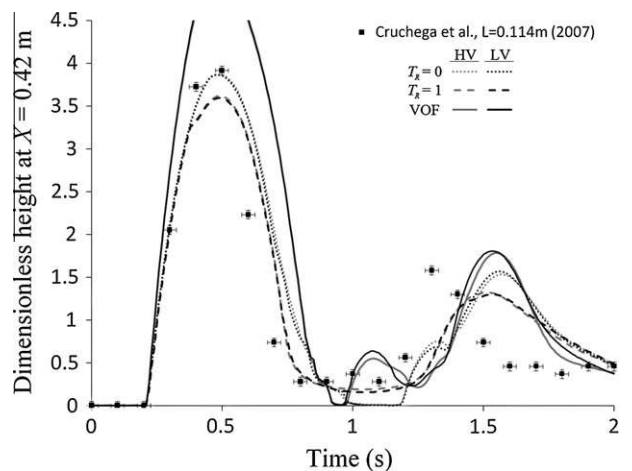


Fig. 10. Dimensionless height,  $Y/L$ , of a collapsing water column at  $X = 0.42 \text{ m}$ .

little to no smearing of the  $0.01 \leq \phi \leq 0.05$  region in the  $T_R = 0$  simulations. At  $T_R = 1$ , significant smearing of this region occurred as the interface travelled up and down the wall, introducing small gradients in  $\phi$  in the gas phase that caused the formation of large vortices. The vortices generated instabilities as the liquid travelled

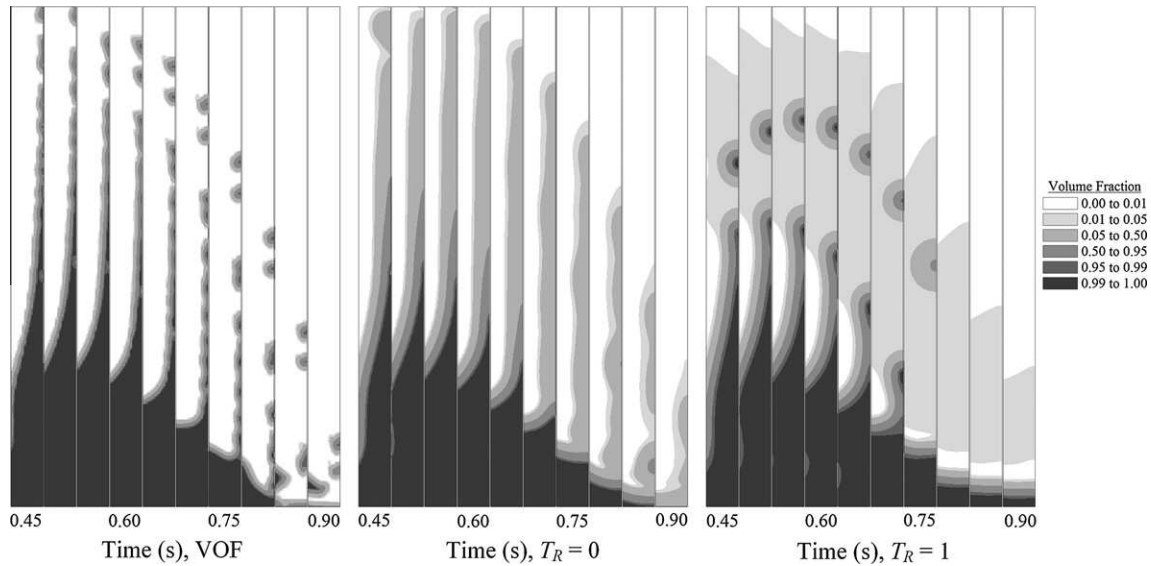


Fig. 11. Temporal evolution of  $\phi$  following the contact of a collapsing column with a wall at  $X = 0.42$  m for VOF (left),  $T_R = 0$  (middle) and  $T_R = 1$  (right).

up the wall, resulting in the formation of the single satellite droplet shown in Fig. 11. The droplet then proceeded to gradually disappear due to spontaneous drop shrinkage, forming a metastable mixture while still suspended above the main fluid interface. The density of this mixture eventually caused it to fall to the base of the geometry; however, the mass was diluted until the inertia of the mixture impacting the liquid phase was insufficient to cause a recession from the wall.

In the experiments of Cruchaga et al. (2007), a recession of the interface from the wall was not recorded near  $t = 1$ . The  $T_R = 1$  simulation was also found to predict this behavior, but the similarity was solely due to spontaneous drop shrinkage, not the physical properties of the system. Nonetheless, the results from  $T_R = 1$  did provide insight into the source of the subsequent discrepancies between the experimental and numerical results shown in Figs. 9 and 10. As the interface receded from the wall, surface forces and inertia from droplet impacts resulted in an increase in the dimensionless height at  $X = 0.27$  m, leading to the over-prediction observed in Fig. 9 near  $t = 1$  s for both the VOF and  $T_R = 0$  simulations. Combined with the error introduced by a delay due to increased droplet falling times, the simulations only possessed qualitative similarities to experimental data following the initial impact of the leading edge with the wall at  $X = 0.42$  m. While discrepancies between the numerical predictions and experimental data can be partially accounted for by the absence of turbulence, wall friction, and vertical shear induced by the removal of the initial obstruction, the inclusion of these factors was not required to successfully highlight the effects of the energy function on flow predictions. Likewise, while the solutions obtained at  $T_R = 1$  could be improved through mesh refinement and a reduction in  $\psi$  and  $C_r$ , the purpose of this comparison was to demonstrate the relative performance of each approach at mesh resolutions comparable to those commonly employed for sharp-interface tracking techniques (VOF).

These results illustrate the performance of the VOF model and TVSED function for the case of flow with minimal curvature, negligible surface forces, and little to no viscous shear acting on the interface. As curvature and surface forces are introduced, spontaneous drop shrinkage is expected to be more significant at  $T_R = 1$ , with viscous shear compounding the problem by shearing off the  $0 \leq \phi \leq 0.05$  region. Such a system represents a worst-case scenario for continuity loss, and is embodied in the simulation of a droplet in simple

### 5.5. Droplet in shear

The deformation of a droplet in low Reynolds number simple shear flow has been studied extensively in literature for Newtonian fluids (see reviews by Acrivos, 1983; Rallison, 1984; Stone, 1994). In a surfactant free system operated at low Reynolds numbers, the droplet shape and orientation are dependent on the viscosity ratio of the droplet and suspending medium,  $\lambda_\eta = \eta_d/\eta_s$ , and the capillary number,  $Ca$ , representing the ratio of viscous (shear) force to surface force. For low viscosity ratios,  $\lambda_\eta \rightarrow 0$ , and small deformations,  $Ca \ll 1$ , the final deformation of a droplet is solely a function of  $Ca$ :

$$D \cong Ca = \frac{r_o G \eta_s}{\sigma} \quad (5.7)$$

where  $r_o$  is the initial bubble radius,  $G$  is the shear rate,  $\eta_s$  is the suspending fluid viscosity and  $\sigma$  is the surface tension. The dimensionless deformation parameter,  $D = (l - b)/(l + b)$ , is generally used to quantify the degree of deformation for elliptical droplets, where  $l$  and  $b$  are the lengths along the major and minor axes. This relationship has been confirmed for  $Ca \ll 1$  and  $\lambda_\eta \ll 1$  both experimentally and computationally (Taylor, 1932, 1934; Cox, 1969; Rallison, 1981; Pozrikidis, 1993; Loewenberg and Hinch, 1996).

At higher capillary numbers,  $Ca \gg 1$ , Hinch and Acrivos (1980) assumed that the droplet had a circular cross section, and used slender body theory to predict  $l/r_o$  for a 3D droplet:

$$\frac{l}{r_o} \cong 3.45 Ca^{1/2} \quad (5.8)$$

Hence, the deformation parameter can then be estimated by fitting the predicted value of  $l$  to an ellipsoid, calculating the corresponding minor axis length which would result in a conserved droplet volume:

$$D \cong \frac{(l/r_o) - 1}{(l/r_o) + 1} \quad (5.9)$$

Experiments carried out by Canedo et al. (1993) found that Eq. (5.8) resulted in an over-prediction of droplet deformation due to the presence of an elliptical droplet cross section. For the range of capillary numbers evaluated ( $3 < Ca < 50$ ), they found their deformation data for 3D droplets was well described by:

$$\frac{l}{r_o} = 3.1Ca^{0.43} \quad (5.10)$$

For intermediate capillary numbers and  $\lambda_\eta = O(10^{-7})$ , Rust and Manga (2002) confirmed the validity of Eq. (5.7) up to  $Ca \cong 0.5$ , and Eq. (5.8) for  $Ca > 1$ . At values of  $Ca$  between 0.5 and 1, the majority of measured deformations were below those predicted by Eqs. (5.7), (5.8), and (5.10).

Two-dimensional simulations were carried out within this intermediate capillary number range to maximize viscous shear and droplet deformation, while avoiding the prohibitive mesh resolution required to capture the extremities of a droplet at high capillary numbers. The parameters used for the VOF and TVSED cases were based on the experimental values reported by Rust and Manga (2002) for an air bubble suspended in corn syrup:  $\rho_s = 1360 \text{ kg m}^{-3}$ ,  $\eta_s = 137 \text{ Pa s}$ ,  $\rho_d = 1.2 \text{ kg m}^{-3}$ ,  $\eta_d = 10^{-5} \text{ Pa s}$  and  $\sigma = 0.082 \text{ N m}^{-1}$ . A droplet with radius,  $r_o = 0.001 \text{ m}$ , was initialized in the center of a  $0.01 \text{ m} \times 0.006 \text{ m}$  2D computational domain using Eq. (2.10), and conditioned for 1000 time steps through the solution of Eq. (3.1) with  $C_T = 0.01$ . Following the initial conditioning, a steady-state solution was obtained for a shear rate of  $G = 0.38481 \text{ s}^{-1}$  with  $C_U = 0.005$ , corresponding to a capillary number of  $Ca = 0.6429$ . Mesh independence was confirmed for  $T_R = 0$  through the comparison of results obtained at three mesh resolutions:  $160 \times 96$  cells,  $\psi = 0.000375 \text{ m}$ ;  $320 \times 192$  cells,  $\psi = 0.0001875 \text{ m}$ ; and  $640 \times 384$  cells,  $\psi = 9.375 \times 10^{-5} \text{ m}$ .

The deformation parameter and angle of deformation at each mesh resolution is provided in Table 1, where a 1% variation in the predicted values is observed when the mesh resolution is doubled from  $320 \times 192$  cells to  $640 \times 384$  cells. Under these conditions, both Eqs. (5.7) and (5.8) predicted a deformation parameter of  $D = 0.6429$ , Eq. (5.10) predicted a value of  $D = 0.6082$ , and the analysis of Rust and Manga's data (2002) yielded an experimental value of  $D \cong 0.5853$ .

The transient behavior of the deformation parameter obtained with a  $320 \times 192$  mesh resolution is illustrated for a 2D droplet in Fig. 12 for the VOF model and TVSED function at  $T_R = 0$  and  $T_R = 1$ . All three models yielded similar results for the initial deformation, with deviations occurring as significant curvature was introduced on the elongated ends of the air bubble. The VOF model yielded a final deformation of  $D = 0.611$ , close to that predicted by Eq. (5.10), while the deformations predicted at  $T_R = 0$  and  $T_R = 1$  were  $D = 0.587$  and  $D = 0.557$  respectively. The results for the TVSED function approximate the empirical data from Rust and Manga (2002), where both  $T_R = 0$  and  $T_R = 1$  yielded values of  $D$  below those predicted for 3D droplets by Eqs. (5.7), (5.8), and (5.10). The source of the discrepancy between the  $T_R = 0$  and  $T_R = 1$  results can be determined from the distribution of  $\phi$  within the computational domain. The contours of  $\phi$  at  $t = 9 \text{ s}$  are shown in Fig. 13 for  $T_R = 1$  (left) and  $T_R = 0$  (right). As the droplet deformed, shear along the edges of the interface smeared the  $0 \leq \phi \leq 0.05$  region in the  $T_R = 1$  simulation, causing a loss in continuity and an apparent decrease in the equivalent initial drop radius,  $r_o$ . As a reduction in  $r_o$  leads to lower values of  $Ca$ , the continuity loss resulted in a lower prediction of the deformation parameter. The  $T_R = 0$  simulation was a true representation of a conservative diffuse interface model,

**Table 1**  
Mesh dependence of the deformation parameter and the angle between the major droplet axis and x-axis at  $t = 9 \text{ s}$  for  $T_R = 0$ .

Mesh resolution	$160 \times 96$ $\psi = 0.000375$	$320 \times 192$ $\psi = 0.0001875$	$640 \times 384$ $\psi = 9.375 \times 10^{-5}$
Deformation	0.5068	0.5899	0.5826
Angle	23.40	20.36	20.59

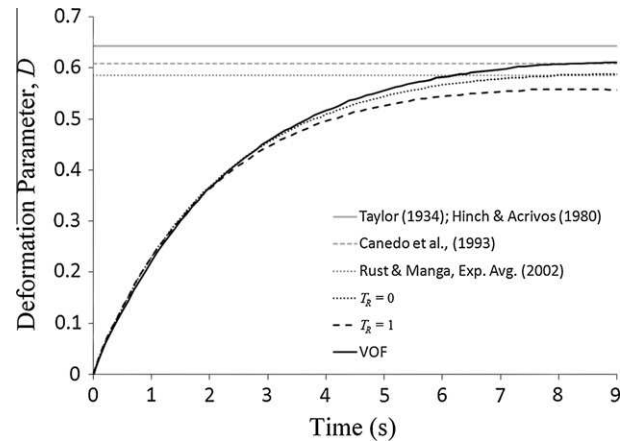


**Fig. 12.** Predicted deformation of an air droplet suspended in corn syrup due to simple shear:  $r_o = 0.001 \text{ m}$ ,  $\lambda_\eta = 7.3 \times 10^{-8}$ ,  $Ca = 0.6429$ ,  $Re = 3.82 \times 10^{-6}$ .

where the  $0 \leq \phi \leq 0.05$  region remained intact and the equivalent initial radius remained constant.

After the bubble reached a stable shape in each simulation, the shear flow was removed and the bubble was allowed to relax to its original shape. Fig. 14 illustrates the variation in the bubble shape during relaxation by plotting the normalized major axis length,  $(l - r_o)/(l_o - r_o)$ , versus  $t/\tau$ , where  $l_o$  is the initial major axis length of the deformed bubble, and  $\tau$  is the surface tension time scale or characteristic relaxation time (Toramaru, 1988; Guido and Greco, 2001):

$$\tau = \frac{r_o \eta_s}{\sigma} \quad (5.11)$$

For an air bubble in corn syrup,  $\tau \cong 1.67 \text{ s}$ . Rust and Manga (2002) also provided an exponential fit for their experimental data, where the shape of a relaxing droplet was approximated by:

$$\frac{l - r_o}{l_o - r_o} = e^{-0.67(t/\tau)} \quad (5.12)$$

The variation in bubble shape for  $T_R = 0$  was almost identical to experimental values reported for similar initial radii. While the VOF model closely matched Eq. (5.12) during the initial relaxation, the formation of spurious velocity currents resulted in a slower relaxation rate as the droplet neared its original shape. For  $T_R = 1$ , the relaxation rate was slightly over-predicted due to smearing of the interface and continuity loss as the initially rapid contraction of the bubble occurred. The smeared region was eventually restored, where the slower relaxation rate from  $t/\tau = 2$  to  $4$  was the result of a gradual reversal of the continuity loss observed shortly after shear flow was removed. This behavior can be seen in Fig. 15, where the percentage continuity loss of the  $T_R = 1$  simulation is reduced from 1.56% at  $t = 2\tau$  to 1.48% at  $t = 4\tau$ , representing approximately 50% of the continuity loss that occurred after the shear flow was removed. It is noteworthy that continuity loss was negligible throughout deformation and relaxation at  $T_R = 0$ , highlighting the advantages of  $T_R = 0$  over  $T_R = 1$  for simulating shear flow.

## 6. Concluding remarks

This paper explored the energy dependency of the three mechanisms responsible for continuity loss for a range of quadratic simplified energy densities described by the TVSED function. The existing limitations of the DI approach were illustrated through the solution of three scalar transport benchmark cases solved at  $T_R = 0$  and  $T_R = 1$ : perceived continuity loss of a quiescent droplet (Section 5.1), spontaneous merging of adjacent droplets (Section 5.2), and continuity

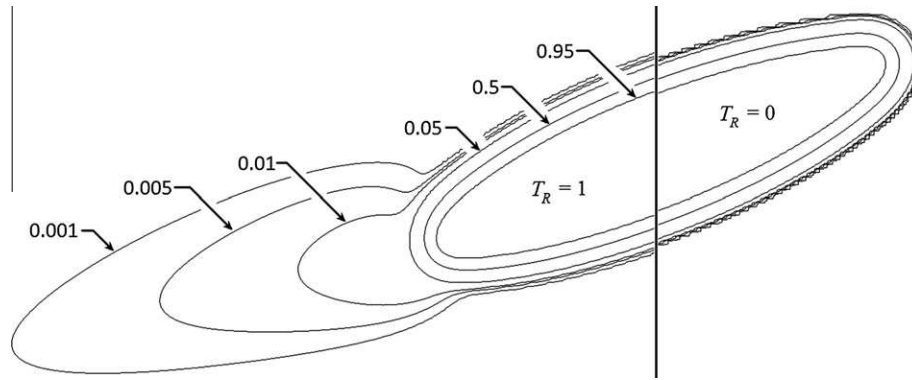


Fig. 13. Contours of  $\phi$  at  $t = 9$  s for the simulation of an air bubble under shear, carried out using the TVSED function at  $T_R = 0$  (right) and  $T_R = 1$  (left).

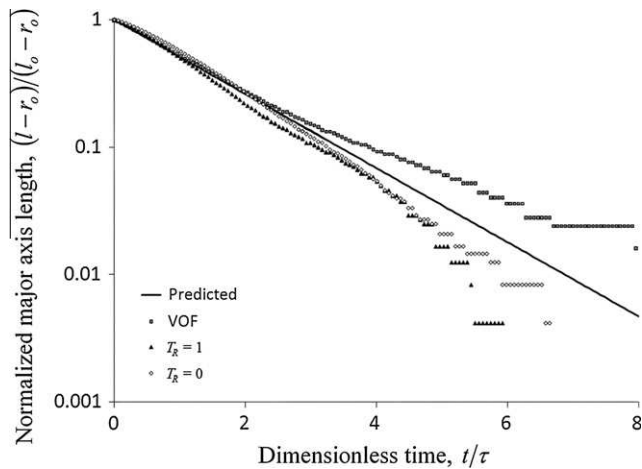


Fig. 14. The relaxation of an air bubble's shape after shear flow is ceased for VOF and TVSED simulations:  $r_0 = 0.001$  m,  $\lambda_\eta = 7.3 \times 10^{-8}$ ,  $Ca = 0.6429$ ,  $Re = 3.82 \times 10^{-6}$ . Predicted values are based on the empirical fit to experimental data reported by Rust and Manga (2002).

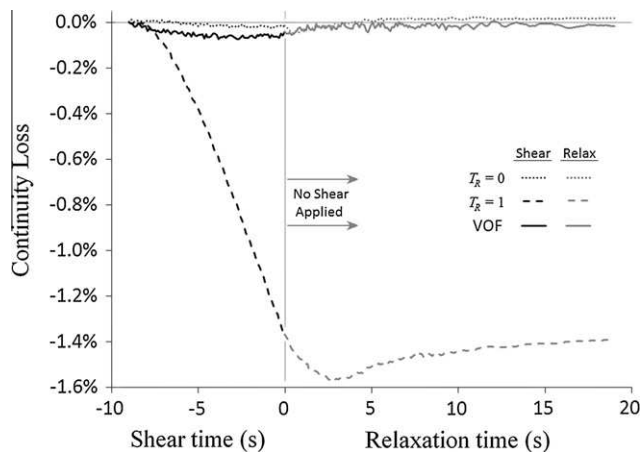


Fig. 15. Continuity loss during droplet deformation in shear and subsequent relaxation for VOF and TVSED based simulations of an air bubble suspended in corn syrup.

loss during scalar transport (Section 5.3). In brevity, free energy analysis and scalar transport simulations in Section 5.1 and Section 5.3 illustrated the elimination of spontaneous drop shrinkage as  $T_R \rightarrow 0$ , where interfacial smearing during convection was significantly reduced due to the absence of a metastable thermodynamic region. The independence of spontaneous drop shrinkage and

convective smearing was confirmed through diagonal convection simulations of partially and fully relaxed initial conditions, as illustrated by the overlap of convective continuity losses shown in Fig. 5. At  $T_R = 0$ , continuity loss was minimized, the adsorption of adjacent droplets through the metastable region was eliminated, and the mobility parameter could be selected based on temporal stability constraints instead of continuity-based constraints.

Two typical two-phase flow benchmark simulations were solved to compare the performance of the proposed DI method at  $T_R = 0$  and  $T_R = 1$  to that of the VOF approach. The collapsing column simulation shown in Fig. 11 illustrated the similarities between VOF and  $T_R = 0$  results with minimal mesh refinement, while providing a clear example of spontaneous drop shrinkage impacting interfacial behavior at  $T_R = 1$ . Simulations of droplet deformation and relaxation in simple shear flow highlighted the performance improvements of the proposed approach. At  $T_R = 1$ , continuity losses caused by portions of the interface shearing away resulted in an under-prediction of the deformation parameter and an inconsistent droplet relaxation rate. In contrast, continuity was conserved at  $T_R = 0$ , with the predicted droplet deformation and relaxation rates in reasonable agreement with empirical data reported by Rust and Manga (2002). While mesh refinement and a reduction in  $\psi$  and  $C_I$  would yield improved results at  $T_R = 1$ , the purpose of this comparison was to demonstrate the relative performance of each approach at mesh resolutions comparable to those commonly employed for sharp-interface tracking techniques (VOF).

This work has effectively eliminated the continuity-loss mechanisms responsible for the constraints placed on the mobility parameter and interfacial width, thereby reducing the mesh requirements in 2D and 3D simulations and improving the overall performance of the DI method. As such, the relative performance of the proposed implementation has been discussed for each two-phase benchmark case, rather than the detailed physics involved. Nonetheless, the proposed TVSED function was implemented and validated in a fully parallelized math-based 3D unstructured mesh solver with adaptive meshing capabilities, and can be extended to multi-phase flow in complex 3D geometries.

**Acknowledgements**

One of the authors (A.A. Donaldson) would like to acknowledge the support of the National Research Council of Canada (NRC) and the Natural Sciences and Engineering Research Council of Canada (NSERC).

**Appendix A. Supplementary material**

Supplementary data associated with this article can be found, in the online version, at doi:10.1016/j.ijmultiphaseflow.2011.02.002.

## References

- Acrivós, A., 1983. The breakup of small drops and bubbles in shear flows. 4th Int. Conf. on Physicochemical Hydrodynamics, vol. 404. Ann. NY Acad. Sci., pp. 1–11.
- Anderson, D.M., McFadden, G.B., Wheeler, A.A., 1998. Diffuse-interface methods in fluid mechanics. *Annu. Rev. Fluid Mech.* 30, 139–165.
- Badalassi, V.E., Cenicerós, H.D., Banerjee, S., 2003. Computation of multiphase systems with phase-field models. *J. Comput. Phys.* 190, 371–397.
- Bonet, J., Kulasegaram, S., Rodríguez-Paz, M.X., Profit, M., 2004. Variational formulation for the smooth particle hydrodynamics (SPH) simulation of fluid and solid problems. *Comput. Meth. Appl. Mech. Eng.* 193, 928–948.
- Cahn, J., Hilliard, J., 1958. Free energy of nonuniform system I. *J. Chem. Phys.* 28, 258.
- Cahn, J., Hilliard, J., 1959. Free energy of nonuniform system III. *J. Chem. Phys.* 31, 688.
- Canedo, E.L., Favelukis, M., Tadmor, Z., Talmon, Y., 1993. An experimental study of bubble deformation in viscous liquids in simple shear flow. *AIChE* 39, 553–559.
- Cox, R.G., 1969. The deformation of a drop in a general time-dependent fluid flow. *J. Fluid Mech.* 37, 601–623.
- Cruchaga, M.A., Celentano, D.J., Tezduyar, T.E., 2007. Collapse of a liquid column: numerical simulation and experimental validation. *Comput. Mech.* 39, 453–476.
- De Menech, M., 2006. Modeling of droplet breakup in micro-fluidic T-shaped junction with a phase-field model. *Phys. Rev. E* 73, 031505.
- Ding, H., Spelt, P.D.M., Shu, C., 2007. Diffuse interface model for incompressible two-phase flows with large density ratios. *J. Comp. Phys.* 226, 2078–2095.
- Feng, J.J., Liu, C., Shen, J., Yue, P., 2005. An energetic variational formulation with phase field methods for interfacial dynamics of complex fluids: advantages and challenges. In: Calderer, M.-C.T., Terentjev, E. (Eds.), *Modeling of Soft Matter*. Springer, New York, pp. 1–26.
- Guido, S., Greco, F., 2001. Droplet shape under slow steady shear flow and during relaxation. Experimental results and comparison with theory. *Rheol. Acta* 40, 176–184.
- Hinch, E.J., Acrivos, A., 1980. Steady long slender droplets in two-dimensional straining motion. *J. Fluid Mech.* 98, 305–328.
- Inamuro, T., Ogata, T., Tajima, S., Konishi, N., 2004. A lattice Boltzmann method for incompressible two-phase flows with large density differences. *J. Comput. Phys.* 198, 628–644.
- Jacqmin, D., 1999. Calculation of two-phase Navier–Stokes flows using phase-field modeling. *J. Comput. Phys.* 155, 96–127.
- Jacqmin, D., 2004. Onset of wetting failure in liquid–liquid systems. *J. Fluid Mech.* 517, 209–228.
- Khatavkar, V.V., Anderson, P.D., Neijer, E.H., 2007. Capillary spreading of a droplet in the partially wetting regime using a diffuse-interface model. *J. Fluid Mech.* 572, 367–387.
- Kim, M.S., Lee, W.I., 2003. A new VOF-based numerical scheme for the simulation of fluid flow with free surface. Part I: New free surface-tracking algorithm and its verification. *Int. J. Numer. Meth. Fluids* 42, 765–790.
- Kim, J., 2005. A continuous surface tension force formulation for diffuse-interface models. *J. Comput. Phys.* 204, 784–804.
- Kim, J., 2007. Phase-field computations for ternary fluid flows. *Comput. Meth. Appl. Mech. Eng.* 196, 4779–4788.
- Koshizuka, S., Oka, Y., 1996. Moving-particle semi-implicit method for fragmentation of incompressible fluid. *Nucl. Sci. Eng.* 123, 421–434.
- Langer, J.S., Baron, M., Miller, H., 1975. New computational method in theory of spinodal decompositions. *Phys. Rev. A* 11, 1417.
- Loewenberg, M., Hinch, E.J., 1996. Numerical simulations of concentrated emulsions. *J. Fluid Mech.* 321, 395–419.
- Martin, J., Moyce, W., 1952. An experimental study of the collapse of liquid columns on a rigid horizontal plane. *Philos. Trans. R. Soc. Lond.* 244, 312–324.
- Oono, Y., Puri, S., 1988. Study of phase-separation dynamics by use of cell dynamical system. I. Modeling. *Phys. Rev. A* 38, 434.
- Pozrikidis, C., 1993. On the transient motion of ordered suspensions of liquid drops. *J. Fluid Mech.* 246, 301–320.
- Rallison, J.M., 1981. A numerical study of the deformation and burst of a viscous drop in general shear flows. *J. Fluid Mech.* 109, 465–482.
- Rallison, J.M., 1984. The deformation of small viscous drops and bubbles in shear flows. *Annu. Rev. Fluid Mech.* 16, 45–66.
- Rust, A.C., Manga, M., 2002. Bubble shapes and orientations in low Re simple shear flow. *J. Colloid Interf. Sci.* 249, 476–480.
- Sochnikov, V., Efrima, S., 2003. Level set calculations of the evolution of boundaries on a dynamically adaptive grid. *Int. J. Numer. Meth. Eng.* 56, 1913–1929.
- Stone, H.A., 1994. Dynamics of drop deformation and breakup in viscous fluids. *Annu. Rev. Fluid Mech.* 26, 65–102.
- Takada, N., Tomiyama, A., 2006. A numerical method for two-phase flow based on a phase field model. *JSME Int. J. B* 49, 636–644.
- Takada, N., Misawa, M., Tomiyama, A., 2006. A phase-field method for interface-tracking simulation of two-phase flows. *Math. Comput. Simul.* 72, 220–226.
- Taylor, G.I., 1932. The viscosity of a fluid containing small drops of another fluid. *Proc. R. Soc. Lond. Ser. A* 138, 41–48.
- Taylor, G.I., 1934. The formation of emulsions in definable fields of flow. *Proc. G. Soc. Lond. Ser. A* 146, 790–796.
- Toramaru, A., 1988. Formation of propagation pattern in two-phase flow systems with application to volcanic eruptions. *Geophys. J. R. Ast. Soc.* 95, 613–623.
- Yuan, P., Schaefer, L., 2006. Equations of state in a lattice Boltzmann model. *Phys. Fluids* 18, 042101.
- Yue, P., Lin, C.L., Patel, V.C., 2003. Numerical simulation of unsteady multidimensional free surface motions by level set method. *Int. J. Numer. Meth. Fluids* 42, 853–884.
- Yue, P., Feng, J.J., Liu, C., Shen, J., 2004. A diffuse-interface method for simulating two-phase flows of complex fluids. *J. Fluid Mech.* 515, 293–317.
- Yue, P., Feng, J.J., Liu, C., Shen, J., 2005. Viscoelastic effects on drop deformation in steady shear. *J. Fluid Mech.* 540, 427–437.
- Yue, P., Zhou, C., Feng, J.J., 2007. Spontaneous shrinkage of drops and mass conservation in phase-field simulations. *J. Comp. Phys.* 223, 1–9.
- Zhou, C., Yue, P., Feng, J.J., Ollivier-Gooch, C.F., Hu, H.H., 2010. 3D phase-field simulations of interfacial dynamics in Newtonian and viscoelastic fluids. *J. Comput. Phys.* 229, 498–511.